

Extraction of relevant physical parameters from 3D images of foams obtained by X-ray tomography

Jérôme Lambert^{a,*}, Isabelle Cantat^a, Renaud Delannay^a, Anne Renault^a, François Graner^b, James A. Glazier^c, Igor Veretennikov^c, Peter Cloetens^d

^a G.M.C.M. Université Rennes 1, UMR CNRS 6626 Bâtiment 11A, Campus Beaulieu, 35042 Rennes Cedex, France

^b LSP, UMR 5588, 140 Avenue de la physique, BP 87, 38402 Saint Martin d'Hères, France

^c Department of Physics, Swain Hall West 159, Indiana University, 727 East Third Street, Bloomington, IN 47405-7105, USA

^d Imaging Group, ESRF, BP 220, 38043 Grenoble Cedex 9, France

Received 4 November 2004; accepted 6 January 2005

Available online 1 February 2005

Abstract

3D liquid foams are investigated for the first time through X-ray tomography. This method enables to observe large number of bubbles (several thousands), and hence, to extract significant statistical characteristics of the foam structure. This article presents the successive steps we followed to achieve this purpose: image acquisition, image processing and data extraction. This global procedure can be automatized, but we emphasize the importance of the choice of two parameters which can be arbitrarily set by users. The first one is the cut-off value for the size of the smallest bubbles, the second deals with the definition of the neighbors of a bubble which is ambiguous for wet foams. We discuss here the consequences of these two choices on characteristics such as the average number of faces of bubbles.

© 2005 Published by Elsevier B.V.

PACS: 42.30.Wb; 81.70.Tx; 82.70.Rr; 83.80.Iz

Keywords: Image processing; Tomography; 3D liquid foams

1. Introduction

Liquid foams are made of thin liquid films separating gas bubbles and of so-called *plateau borders* connecting these films in a continuous network, and containing the largest part of the fluid phase. In situ observation of such a structure is a challenge, even more during dynamical processes like ageing or flowing, because of the high diffusivity of the foam and of the small amount of matter involved. Recently, MRI experiments allowed to visualise the plateau border network of a liquid foam [1,2]. Optical tomography has also been used to observe the foam structure and to follow several individual bubbles in their ageing process [3,4]. Nevertheless, the foam properties are intrinsically statistical and their determination

imposes the study of a large number of bubbles which was not possible with these techniques. Recent improvements of X-ray micro-tomography at the European Synchrotron Radiation Facility (ESRF, ID19 beamline) and of 3D image analysis allowed us to obtain images of a liquid foam during drainage and coarsening, with a number of bubbles larger than in previous works. Segmentation of the image into a set of well-identified individual bubbles is proved to be feasible automatically despite the large amount of missing thin films in the image of the structure. Statistical properties of the structure, as bubble volume distribution, number of neighbors, liquid fraction can thus be extracted from the image. This article presents the fast image acquisition procedure using synchrotron radiation at the ESRF. Then, the image segmentation is described and some preliminary results on the foam structure at a given time are discussed. The characterisation of the foam evolution, allowed by this technique, will be the aim of a future work.

* Corresponding author. Tel.: +33 299 388 601; fax: +33 223 236 717.

E-mail address: jerome.lambert@univ-rennes1.fr (J. Lambert).

2. Image acquisition

2.1. Sample preparation

The size of the volume scanned by the X-ray beam is 1 cm^3 . The foam contained in this volume must be stable enough to obtain good quality images, but should evolve significantly during the experiment (some hours), and initially hold a large number of bubbles to be statistically relevant.

The experimental cell is made out of a hollow acrylic cylinder (see sketch in Fig. 1). Air is injected in this cell through a porous plate imbedded with a foaming liquid. We thus obtain a relatively mono-disperse foam.

Three distinct ageing mechanisms are involved in the evolution of a liquid foam: gas diffusion across the liquid films, liquid drainage and film rupture. The ingredients involved in the making of the foam were chosen in order to inhibit the film rupture and the drainage and to focus on the gas diffusion mechanism (“coarsening”). These ingredients were, for 100 mL de-ionised water:

- 0.1 g sodium dodecyl phosphate,
- 0.003 g dodecanol, and
- 1 g gelatine.

In addition, we set the liquid fraction of the foam to a large value ($\approx 10\%$) and keep it constant by maintaining a continuous liquid flow throughout the cell during the experiment, which balances the effect of the drainage. The cell is nearly transparent to X-rays and allows to acquire a large number of radiographs corresponding to different angular settings as needed for tomographic reconstruction.

2.2. X-ray micro-tomography

Third-generation synchrotron X-ray sources provide partially coherent, homogeneous and very bright photon beams. Here, we mainly exploit the possibility to image with a high temporal resolution. Propagation-based phase contrast allows furthermore to enhance the contrast for structures with weak attenuation such as thin liquid films. At the experimental sta-

tion ID19 of the ESRF used for the experiments, the energy of the synchrotron beam is set to 15 keV by a double silicon crystal monochromator. Radiographs for 900 angular settings over a 180° range are recorded with a CCD-based high resolution detector system. It uses a high quality Peltier-cooled CCD (ESRF FReLoN camera) with 14-bit dynamic range and 1024×1024 pixels. The read-out time for a single frame is 65 ms. The X-ray signal is converted into visible light by a $10 \mu\text{m}$ thick $\text{Gd}_2\text{O}_2\text{S:Tb}$ converter screen. The effective pixel size is $10 \mu\text{m}$ with a corresponding field of view of 10 mm. The exposure time for a single radiograph was set to 50 ms. The closing time of the mechanical shutter introduces further an overhead resulting in a total acquisition time of 150 s for one tomographic scan. The sample-to-detector distance is set to 130 mm. The recorded radiographs contain therefore both attenuation- and propagation-based phase contrast. Nevertheless, the reconstruction procedure for absorption tomography based on the filtered back-projection algorithm [5,6] was used to combine the set of 900 radiographs into a 3D image. It can be shown [7] that, if the sample-to-detector distance is small, the reconstruction is the sum of two contributions: the usual attenuation coefficient μ and a second term equal to $-D \Delta \delta(x, y, z)$. δ , the refractive index decrement, is proportional to the electron density of the scanned material, and D is a proportionality coefficient. The Laplacian operator will therefore enhance the visibility of structures related to abrupt changes in density (edges, thin films, etc.). A large number of 3D images were recorded during 38 h: the exposure time

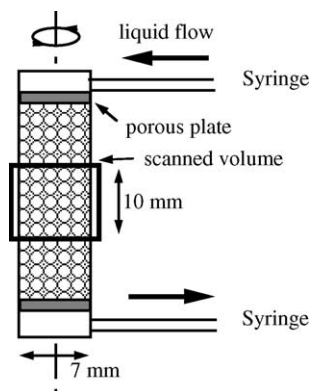


Fig. 1. Sketch of the experimental apparatus.

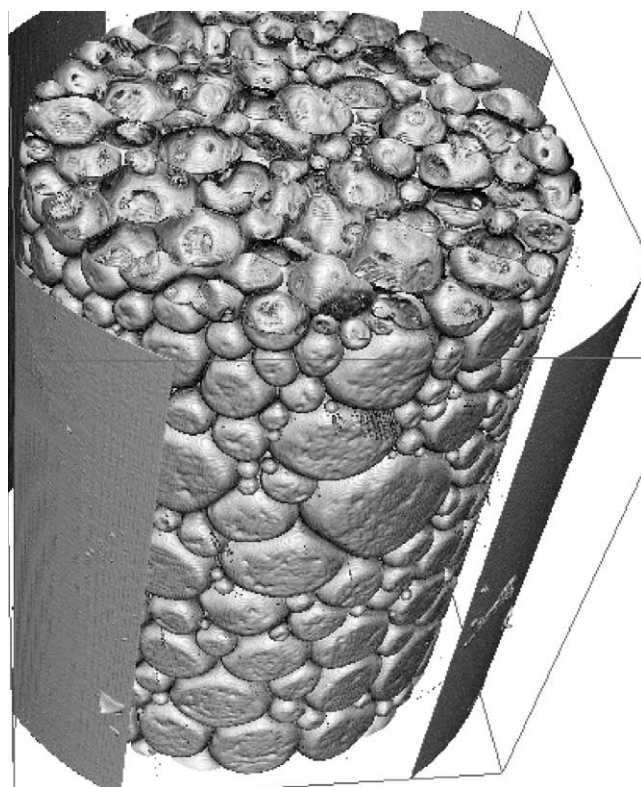


Fig. 2. 3D view of the liquid foam.

was 2.5 min, and the minimum time between two images was 8 min.

3. Image analysis

The reconstructed volumes contain $850 \times 850 \times 1024$ (respectively, in x , y and z directions) voxels and are coded on 8 bits (hereafter “grey level” images: the pixels are labelled from 0 (black) to 255 (white)). Fig. 2 shows a 3D rendering showing an isodensity map of a typical image. The real size of the volume is $8.5 \text{ mm} \times 8.5 \text{ mm} \times 10 \text{ mm}$. One clearly distinguishes the bubbles on this figure, as well as the external wall of the cylinder. This image shows that it should be possible to segment the image and identify the different bubbles. However, this procedure is not performed straightforwardly either by the human eye—because of the very large amount of bubbles that have to be numbered and described—nor by computer-assisted image analysis for reasons that will be addressed in this section.

Let us first describe the main qualitative features appearing on different slices of the foam. Fig. 3 shows four slices

extracted from images obtained at two different stages of the coarsening. The bi-phasic nature of the foam is still obvious on each slice. Thus, the shapes of the 2D sections of the bubbles are easily readable. In the early stages of the coarsening ($t = 71 \text{ min}$ after the making of the foam), the bubbles (in dark) appear to be round. Their mean size varies along the height of the cylinder as can be seen by comparing the top and bottom slices in Fig. 3. In later stages (e.g. for $t = 38 \text{ h } 40 \text{ min}$), the bubbles seem to adopt the shapes of polyhedra.

On the other hand, one may point out the fact that the intensity fluctuates in both phases. This is clear from Fig. 4, where the frequency of the different intensities is plotted for a circular area of radius = 350 voxels drawn on the top left slice pictured in Fig. 3. The first peak, centred on intensity level 97, is due to the gaseous phase (bubbles), whereas the very smooth plateau ranging from intensity levels 130 to 250 is the signature of the most absorbing phase, i.e. the liquid phase contained in the plateau borders and in the films. Let us discuss the possible origin for this spreading of the peaks.

One may first exclude the electronic noise or artefacts of the camera and of the experimental apparatus. This is made clear by the fact that if one considers the frequency of the

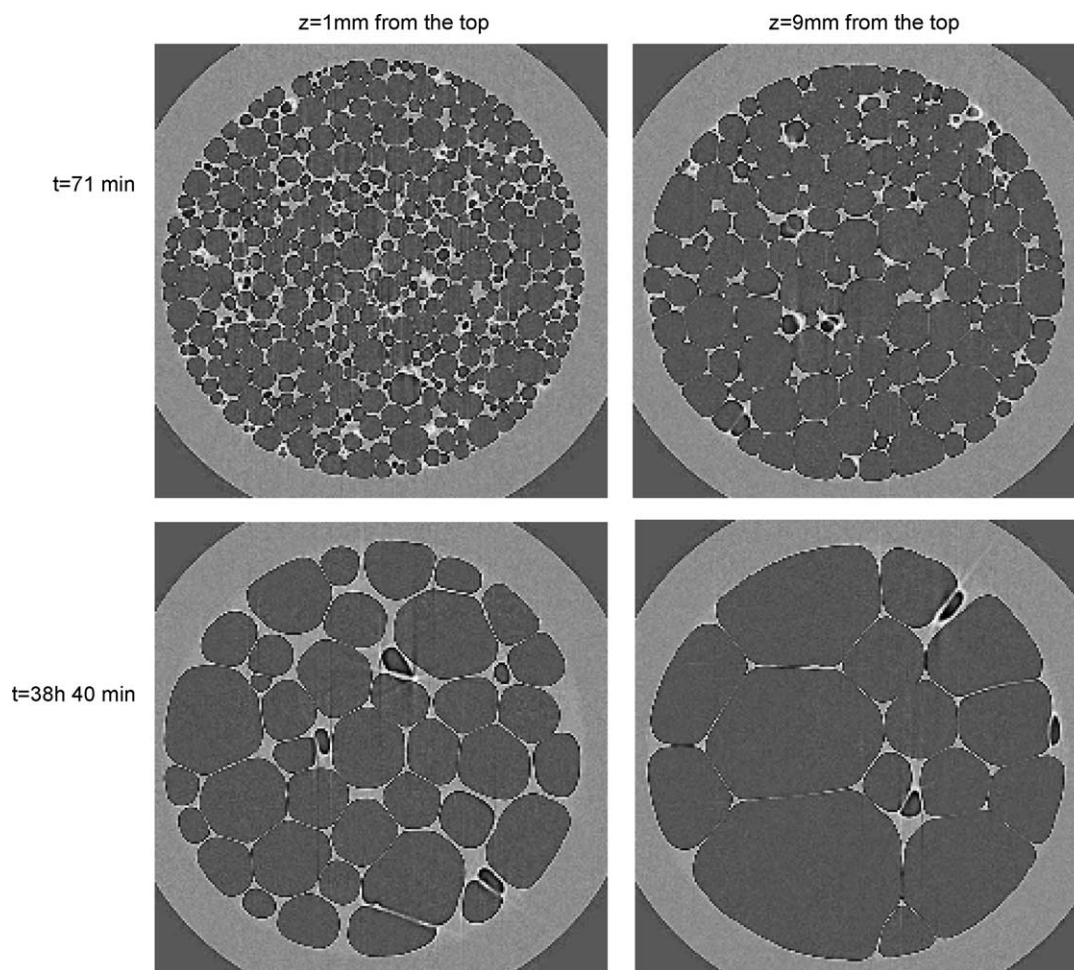


Fig. 3. Four slices recorded at 1 mm (left) and 9 mm (right) from the top of the scanned volume, 71 min (top images) and 38 h 40 min (bottom images) after the making of the foam.

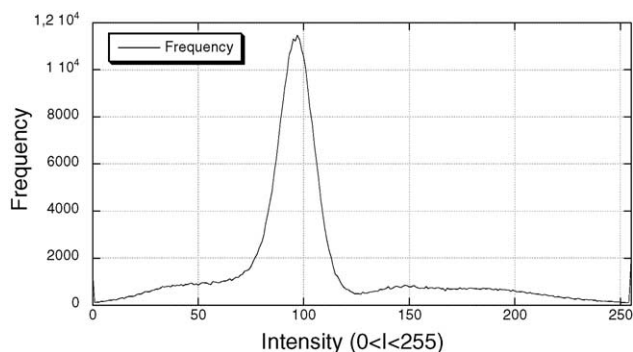


Fig. 4. Intensity frequency histogram of the grey levels of the voxels contained in a circular area (radius = 350 voxels) of the first slice pictured in Fig. 3.

intensity of the voxels outside the cylinder (i.e. in the corners of the slices shown in Fig. 3), the intensity is found strictly constant (equal to 99) as long as one does not take into account the voxels nearest to the wall of the cylinder. On the contrary, one may spot large intensity variations in Fig. 5 which represents a detail of the top left slice shown in Fig. 3. This is made clearer in Fig. 5(b), where the intensity profile along the white segment of Fig. 5(a) is shown. The wet plateau border crossed by the segment has a clear signature on this profile, whereas the film is hardly recognisable. Actually, the spreading of the peaks on the histogram pictured in Fig. 3 is mainly due to two factors that will intervene during the image reconstruction procedure:

- (1) The non-local character of the grey level intensity recorded for each voxel. Indeed, the grey level intensity of a voxel is deduced from a filtered back projection of a set of radiographs. The radiographs have a finite pixel size and are blurred due to the detector response. Moreover, each original pixel mixes both local (absorption) and non-local (phase contrast) informations.
- (2) The dynamics of the foam. Each image acquisition lasts for about 2 min for this set of experiments. For example, a film breaking during this acquisition will result in a bad fit between the different radiographs which will not correspond to the same 3D structure anymore. This results locally into a variation of the intensity gradient on the images and into a deformation of the apparent shapes of the bubbles. Of course, other dynamical phenomena such as coarsening or film vibrations may provoke similar results.

Thus, it is difficult to rely on the variations of the contrast in a phase to characterise its homogeneity. In addition, the phase boundaries are considerably enhanced since the original 2D radiographs contain phase information related to the local density variations; thus, it is very unlikely that the grey level scale will provide any quantitative information about the thickness of the films. Therefore, we shall rely here only on the information provided by segmented images, where the two phases are separated. In the follow-

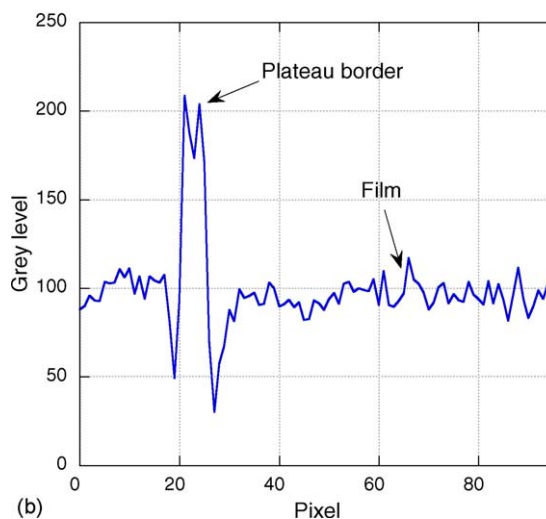
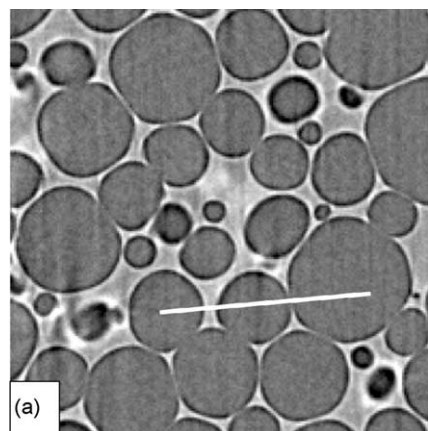


Fig. 5. (a) Detail (200×200 voxels in size) of the first slice shown in Fig. 3. (b) Intensity profile along the white segment shown in (a).

ing section, we will describe the way the segmentation is performed.

3.1. Extraction of the relevant parameters for a physical analysis

The segmentation process is based on our knowledge of the basic structural characteristics of a foam: first, the liquid phase is continuous. In addition, each plateau border is prolonged by a film although this latter might not be visible. We also neglect the very small inclusions of each phase into the other. Liquid drops of a few voxels in suspension into a bubble are necessarily artefacts. Small bubbles of the same order of size may be real but are unreliable, as they can be confused with noise induced by the reconstruction process. We will further address the consequences of this important hypothesis.

The segmentation process is performed using the commercial software Aphelion, which includes a set of dedicated 3D libraries. A first step of the segmentation process consists in obtaining a thresholded image to separate both phases. The contrast is first enhanced by using a non-linear $3 \times 3 \times 3$

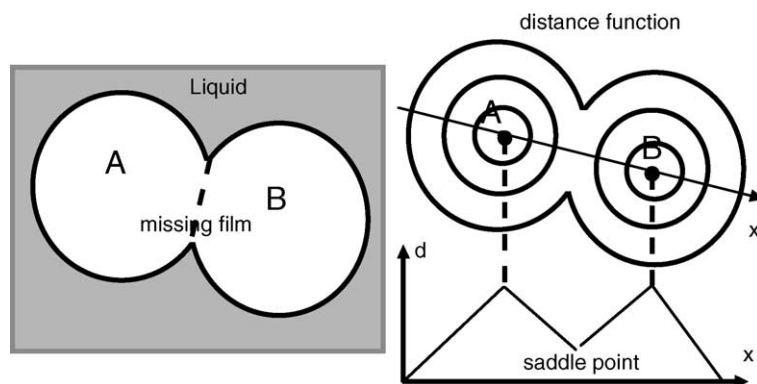


Fig. 6. Left: sketch of two artificially merged bubbles. Right: distance function to the liquid phase. The lines are iso-distance levels. The “•” symbols designate the local maxima of the distance function.

median filter. The image is then thresholded. The threshold level is set so as to minimise the number of lonely voxels in each phase. Let us underline the fact that the value of the threshold is stable from one slice to another, on the same or on successive images.

The threshold procedure may have erased the films separating the different bubbles since some films are too thin to be detected. One must notice that this is not important in order to compute the liquid fraction in the foam since the liquid is mainly contained in the plateau borders, but is especially important in order to separate the different bubbles. Thus, these films must be re-built. This is achieved by applying the procedure described hereafter, based on the fact that the polyhedron defined by each bubble’s plateau borders should be convex: two bubbles are separated by a film and a few plateau borders. If a film F separating two bubbles A and B is missing on the image, A and B will artificially be merged into a single large bubble C . C should be cut in two parts. As the superficial tension tends to diminish the surface of F , the signature of the missing film arises from the narrowing of the bubble C , which exhibits a “peanut” shape (see Fig. 6). This effect is quantified by the distance map between each voxel and the nearest point belonging to the liquid phase. For example, in the simple case pictured in Fig. 6, the artificial bubble C has a map with two maxima, whereas A and B should each have one maximum in this example. The voxels localised in the missing film are relatively close to the plateau borders surrounding F . This results in the appearance of a “saddle” point on the distance map. This saddle point indicates the place where C should be cut. Let us notice that this method provides us a convenient way to split C at a place located near the original film but not to recover the respective Gaussian curvatures of A and B .

Actually, most bubbles may exhibit several local distance maxima since their shapes are not perfectly convex. In order to avoid to cut these bubbles, one introduces a criterion on the relative variation of the distance function between two maxima in comparison with the maximum value of the distance function for this bubble: thus, if the value of the distance function at the saddle point is larger than a certain fraction

of the maximum distance, the two maxima are considered as belonging to the same bubble. The value of the fraction is optimized manually once and for all the images.

Practically, a first step consists in performing an opening of the image in order to get rid of the lonely voxels. Then, the proper convexity detection, based on the procedure described earlier, is performed by using the “*ImgClusterSplitConvex*” Aphelion native operator. This operator performs three successive operations: a distance function computation, followed by a filtering step in order to eliminate spurious maxima and a cut based on the local maxima method. A parameter, the “strength” of the operator, is set manually to distinguish single bubbles with several distance maxima from artificially merged bubbles using the method described earlier. This procedure gives good results as can be seen in Fig. 7.

The images being quite large (720 Mo), and the previous operators memory consuming, it was necessary with our computer to divide the whole image into 36 subvolumes of

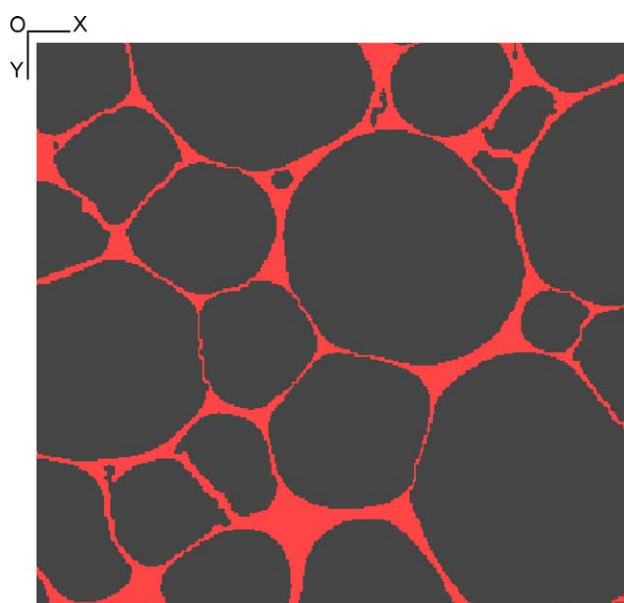


Fig. 7. Detail (200 × 200 voxels in size) of a segmented image.

$283 \times 283 \times 256$ voxels in order to proceed to the segmentation and to the registration of the bubbles.

This segmentation procedure being achieved, it is then possible to register the bubbles and compute their individual geometric characteristics such as their volume, surface and positions.

3.2. Neighborhood

In addition, it is crucial to get some insights about each bubble's neighborhood, i.e. numbering its neighbors and determining the surface shared with each neighboring bubble. This is achieved by making each bubble grow and testing its overlap with the neighboring bubbles: thus, the distance between two bubbles is here defined as the number of *dilate* operations successively applied to a single bubble before it overlaps another bubble. Let us recall here that the *dilate* morphological operator consists in considering that any voxel belongs to a bubble if it is in contact, i.e. inside a $3 \times 3 \times 3$ voxels large cube, a voxel itself belonging to this bubble. The same method was previously used in 2D foams by Lorderau et al. [8] in order to get an automatised determination of the number of neighbors of a large set of bubbles. The amplitude of the growth influences the neighbor's distribution as shown further. Let us notice that in wet foams, a length-scale is given by the diameter of the plateau border section, which provides a natural value for the growth amplitude. An alternative is to build another foam structure, namely the dried foam structure, in order to obtain a definition of the neighborhood independent of any new parameter (but not of the drying procedure).

This dried foam structure is determined by making the bubbles grow at the same rate, starting from their original shape. If two bubble surfaces meet at any point, the growth stops at this point. The growth carries on until the bubbles completely fill the space. Each plateau border is thus reattributed to the surrounding bubbles. The neighborhood is thus clearly defined and is obtained using the previous algorithm with growth amplitude of one. It must be underlined that this method is not the only one that can be used to fill the space starting from the initial configuration. One could use either Voronoi or Laguerre tessellations for example [9].

3.3. Boundary effects

At this point, it is worth underlining the fact that the bubbles that are in contact with the boundaries of the subvolumes may introduce important biases in the statistics of the different characteristics of the bubbles (e.g. volume, neighborhood), since they are cut by the boundaries and sometimes even during the segmentation process.

Thus, we chose, in the work reported in this article, to remove these boundary bubbles from the samples used in the statistics.

Indeed, this method already provides interesting results as will be exposed in the following section. For example,

let us underline the fact that a single subvolume contains almost 2000 bubbles at the beginning of the observation. This represents an interesting quantitative progress with respect to previous results obtained using optical tomography or NMR imaging, where the number of bubbles observed was of the order of 200. It is possible to go further in the segmentation by glueing the subvolumes back using a "shoelace" procedure in order to take into account the bubbles that are cut by the subvolume boundaries. This latter method will be described in a future paper, since the results that are discussed here only concern subvolumes.

3.4. Experimental results and discussion

3.4.1. Liquid fraction

The volume liquid fraction is measured on binary images. It is deduced from the liquid fraction measured on slices ($z = \text{constant}$) or on hollow cylinders (constant radius) in order to get an insight of any spatial inhomogeneity of the liquid repartition in the foam. The influence of the threshold on the value of the liquid fraction deduced at constant height is not crucial: one observes a variation of the order of ± 0.02 of the liquid fraction for thresholds varying between 107 and 113. This is due to the fact that the liquid is mainly contained in the plateau borders for which the voxels are clearly distinct from the voxels of the gaseous phase. For the results described hereafter, we chose a threshold of 110.

The liquid fraction determined by this means varies roughly between 0.1 and 0.2 as can be seen in Fig. 8. This figure shows the variation of the liquid fraction (ϕ_1) as a function of the height z in the cylinder. ϕ_1 was computed for each slice $z = \text{constant}$ by calculating the mean value of the binary voxels inside a circular area of radius 3 mm in the cylinder.

The largest value of ϕ_1 is obtained for $z = 0$, which is the top of the cylinder. Indeed, this means that the drainage is overbalanced by the liquid injected on top of the foam. This "inverted gradient" is maintained during the whole experiment as can be read on the following lines of the same figure. It seems that this inverted gradient is quickly stabilised throughout the foam since $\phi_1(z)$ does not vary very much between 80 min and 38 h after the making of the foam.

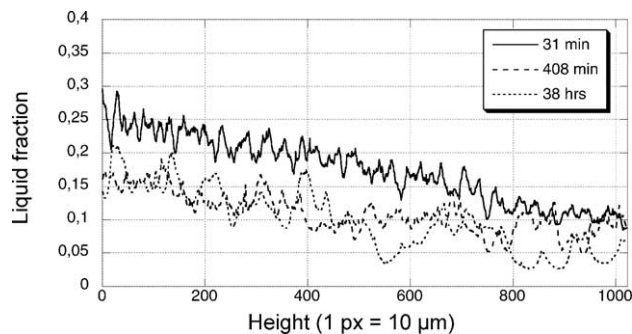


Fig. 8. Variations of the liquid fraction as a function of z , the height in the cylinder, for different stages of the evolution of the foam.

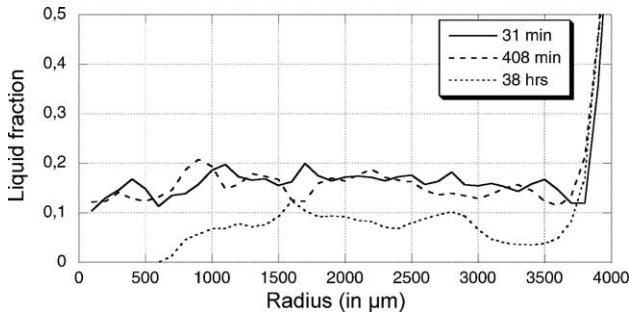


Fig. 9. Variations of the liquid fraction as a function of r , the distance to the axis of the cylinder, for different stages of the evolution of the foam.

One may notice that the first line in Fig. 8 is quite regular whereas later lines fluctuate considerably more. These fluctuations reflect the fact that the mean size of the bubbles increases. Thus, there are less bubbles in the same cylinder at later stages of the foam coarsening. This results of course in greater fluctuations of $\phi_1(z)$.

Fig. 9 shows the evolution of ϕ_1 as a function of r , integrated between heights 800 and 900 (bottom of the cylinder). Even in the early stages of the evolution, it seems that the liquid fraction is constant inside the cylinder except for a small volume close to the wall of the cylinder. One may still see that the average value of ϕ_1 lowers quickly, and that the fluctuations of ϕ_1 are more important at later stages of the evolution.

3.4.2. Bubble size distribution

Let us here describe the results of a detailed analysis on a given subvolume (containing approximately 750 internal bubbles) extracted from an image obtained approximately 80 minutes after the making of the foam. The distribution of the volumes of the bubbles inside this subvolume is shown in Fig. 10. The bin of the histogram is 2000 voxels. One may see that a large region of the distribution can be approximated by an exponential distribution.

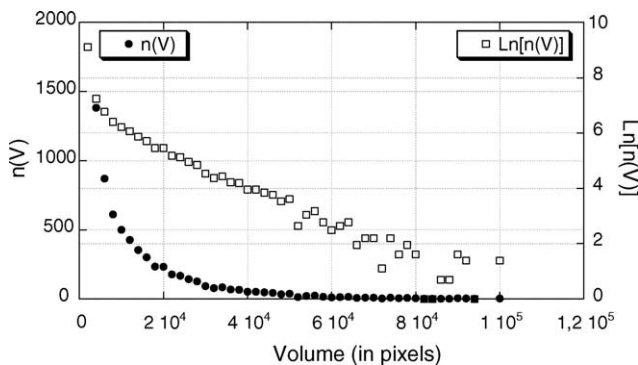


Fig. 10. Frequency histogram of the size of the bubbles contained in a circular area (radius = 350 voxels, height = 256 voxels) corresponding to the fourth of the whole cell volume. (●) Linear representation of the number of bubbles of size V , the bin is set to 2000 voxels; (□) logarithmic representation of the same set.

As previously evoked, it is important for us to know to what extent the small bubbles modify the statistics observed, and on which basis one can purely neglect them. Indeed, small bubbles dominate the size distribution. Some of these small bubbles are spurious bubbles, introduced during the reconstruction or the segmentation process. This does not influence the shape of the size distribution except for small bubbles. In addition, the fact that we only considered bubbles that are completely embedded in the subvolume, introduces a bias toward the small bubbles. This could influence significantly the shape of the distribution if the number of surface bubbles is comparable to the number of volume bubbles. Thus, it is important to work on large samples.

3.4.3. Neighborhood

Following the 2D case, most of the models introduced to describe the coarsening of 3D *dry* foams try to relate the rate of coarsening of individual bubbles or sets of bubbles to their number of faces (see [2,10], Hilgenfeldt et al. and Cox et al. and references therein in this volume). However, it is difficult to define a neighborhood, and hence faces, in a real 3D *wet* foam. One might think the best way to define rigorously the neighborhood is to work with a dried foam, the obtention of which was previously discussed. Yet, in such a foam, there remains no information about the distance separating two neighboring bubbles, the distance between two bubbles being here defined as the number of *dilate* procedures one must apply to a bubble for it to overlap the other bubble. This represents a great difficulty of this approach since this assumes that distant, though neighboring, bubbles may exchange gas with the same rate as two bubbles that are really close to one another. Inversely, some bubbles which are found to be neighbors in the dried foam might be more distant than bubbles which might have exchanged gas but that are not considered as neighbors. Thus, another way to determine whether two bubbles are neighbors or not is to compute their minimal distance. Doing so, one may select a length scale corresponding to the typical size of a plateau border section. Three distributions of number of faces were computed and are compared in Fig. 11: one deduced from the foam obtained using the drying process, the two others obtained from the original foam using the maximal distance criteria $d \leq 2$ and $d \leq 7$ voxels. Whereas for large number of faces, the three distributions are relatively similar, there are discrepancies for small number of faces. Indeed, with the distance criterion, it may happen that bubbles are isolated in the liquid so that they do not have any neighbor (see $d \leq 2$ in Fig. 11)! Of course, this is not possible on dried foams as can be verified on the “dried foam” curve.

As previously mentioned, one has to take into account small spurious bubbles. They are more likely to possess a few neighbors. This results in a change of the distribution of the number of faces. In order to see to what extent this factor plays a role, we show in Fig. 12 the behavior of the average and standard deviation of the distribution as a function of the volume of the smallest bubble taken into account for a

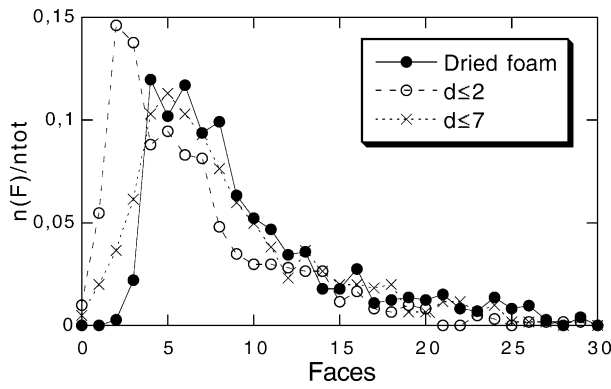


Fig. 11. Three distributions of the number of faces computed for the same set of bubbles. The procedure used to obtain a dried foam is described in the text; $d \leq 2$ (respectively, 7) is the maximum distance in voxels between two bubbles for them to be considered as neighbors.

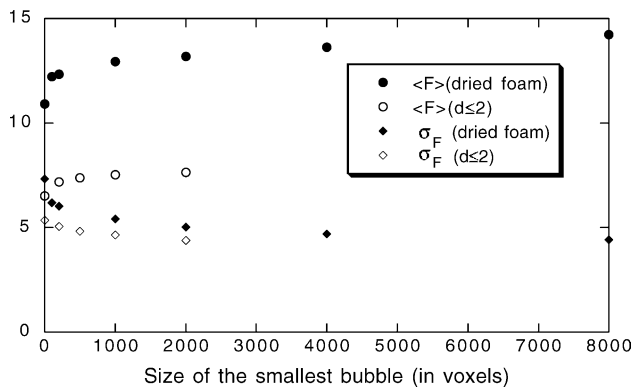


Fig. 12. Average $\langle F \rangle$ (● for the dried foam, ○ for the $d \leq 2$ neighborhood criterion) and standard deviation σ_F (◆ for the dried foam, ◇ for the $d \leq 2$ neighborhood criterion) values of the number of faces as a function of the size of the smallest bubble taken into account in the distribution (in voxels) for a dried foam.

dried foam and for the $d \leq 2$ distance criterion. The influence of the small bubbles is to shift the distribution towards the small number of faces and to widen the distribution. Let us notice that the average number of faces of the dried foam derived from our experimental results is slightly smaller than the average number of faces of foams used in different models (see [11,12]), whereas the average number of faces deduced from the $d \leq 2$ criterion is considerably smaller.

4. Conclusion

In this article, we showed how 3D images of liquid foams were obtained and processed in order to extract relevant informations about the foam structure. The X-ray microtomography technic was described, as well as the procedure used to extract physical informations from subvolume taken from a 3D images. This enabled us to obtain statistics about

a large number of bubbles (≈ 750 on the image shown here) isolated from the walls of the cell, which represents a progress with respect to previous results obtained on 3D foams. We highlighted the influence of two parameters on the statistics obtained from the segmentation process: the first one is the cut-off on the size of the bubbles. The second one deals with the definition of the neighborhood in wet foams.

The perspectives are, on the one hand, the extension of this procedure to the whole volume of the cell in order to increase the sharpness of the statistics, and, on the other hand, the analysis of the behavior of single bubbles, which might provide us useful informations about, amongst other phenomena, the coarsening of the foam.

Acknowledgements

J.L. wishes to thank L. Oger and G. Le Caër for very useful discussions, as well as the technical assistance of the Aphelion team.

References

- [1] C. Gonatas, J. Leigh, A. Yodh, J. Glazier, B. Prause, Magnetic resonance images of coarsening inside a foam, *Phys. Rev. Lett.* 75 (1995) 573–576.
- [2] J.A. Glazier, B. Prause, Current status of the three-dimensional growth laws, in: P. Zitha (Ed.), *Foams, Emulsion and Their Application* (Proceedings of the Eurofoam Conference, Delft 2002), Verlag MIT, Bremen, 2000, p. 120.
- [3] C. Monnereau, M. Vignes-Adler, Optical tomography of real three-dimensional foams, *J. Colloid Interface Sci.* 202 (1998) 45.
- [4] C. Monnereau, M. Vignes-Adler, Dynamics of 3D real foam coarsening, *Phys. Rev. Lett.* 80 (1998) 5228.
- [5] G.T. Herman, *Image Reconstruction From Projections*, Academic Press, New York, 1980.
- [6] P. Cloetens, W. Ludwig, E. Boller, F. Peyrin, M. Schlenker, J. Baruchel, 3D imaging using coherent synchrotron radiation, *Image Anal. Stereol.* 21 Suppl. 1 (2002) S75–S85.
- [7] P. Cloetens, M. Pateyron-Salome, J.Y. Buffiere, G. Peix, J. Baruchel, F. Peyrin, M. Schlenker, Observation of microstructure and damage in materials by phase sensitive radiography and tomography, *J. Appl. Phys.* 81 9 (1997) 5878–5886.
- [8] O. Lordereau, R. Delannay, I. Cantat, J. Lemaître, Characterization of the cellular structure, in: *Proceedings of the Eighth European Congress of Stereology and Image Analysis, Bordeaux 2001*, 2001, pp. 3844–3849.
- [9] G.F. Voronoi, Nouvelles applications des paramètres continus à la théorie des formes quadratiques. deuxième mémoire: recherche sur les parallélogrammes primitifs, *Journal für die reine und angewandte Mathematik* 134 (1908) 198–287.
- [10] J. Stavans, The evolution of cellular structures, *Rep. Prog. Phys.* 56 (1993) 733–789.
- [11] J. Glazier, Grain growth in three dimensions depends on grain topology, *Phys. Rev. Lett.* 70 (1993) 2170.
- [12] J.A. Glazier, D. Weaire, The kinetics of cellular patterns, *J. Phys.: Condens. Matter* 4 (1992) 1867.